

# Analysis of magnetic interactions in rare-earth-doped crystals for quantum manipulation

O. Guillot-Noël,\* Ph. Goldner, and E. Antic-Fidancev

*Ecole Nationale Supérieure de Chimie de Paris (ENSCP), Laboratoire de Chimie Appliquée de l'Etat Solide, CNRS-UMR 7574, ENSCP, 11 rue Pierre et Marie Curie, 75231 Paris Cedex 05, France*

J. L. Le Gouët

*Laboratoire Aimé Cotton, CNRS-UPR 3321, Bâtiment 505, 91405 Orsay Cedex, France*

(Received 1 June 2004; revised manuscript received 4 October 2004; published 12 May 2005)

The influence of magnetic interactions in rare-earth-doped crystals under an external magnetic field has been studied in order to obtain an efficient three-level  $\Lambda$  system with the hyperfine levels of the rare earth. Nuclear Zeeman effect under the action of an external magnetic field removes the nuclear degeneracy. This interaction does not provide an efficient  $\Lambda$  system because nuclear-spin flipping such as  $|M_I\rangle = \pm \frac{1}{2} \rightarrow |M_I\rangle = \mp \frac{1}{2}$  ( $M_I$  is the nuclear-spin projection) cannot be induced by an optical transition. However, this selection rule only applies to pure nuclear Zeeman effect. Indeed, it is shown that the coupling of the electronic Zeeman and of the hyperfine interactions releases the nuclear-spin selection rules  $\Delta M_I = 0$ . This can be described in terms of a pseudonuclear Zeeman effect induced by an effective magnetic field. The relative strengths of the two optical transitions involved in the three-level system can be controlled by the orientation of the external magnetic field. The particular case of the  $\text{Tm}^{3+}$  ion in the  $\text{Y}_3\text{Al}_5\text{O}_{12}$  host (YAG) is discussed.  $\text{Tm}^{3+}$  hyperfine structure is determined using a complete Hamiltonian including free-ion, crystal-field, and magnetic interactions. A good three-level  $\Lambda$  system is obtained in  $\text{Tm}:\text{YAG}$  with a transition strength ratio of 0.24 ( $\sim 1:4$ ) between the two optical transitions. An analytical analysis based on a spin-Hamiltonian approach is proposed to explain the results of the complete crystal-field calculations. Finally, an experimental protocol that makes a crystal similar to the atomic samples used in previous quantum information investigations, with the additional benefits of absence of motion and long coherence time, is described.

DOI: 10.1103/PhysRevB.71.174409

PACS number(s): 42.50.Gy, 71.70.Ej

## I. INTRODUCTION

Quantum physics has long been confined to the description of microscopic scale processes, or to the investigation of very specific macroscopic states of matter such as superfluids, superconductors, or Bose-Einstein condensates. However, there has been growing interest in the investigation of quantum processes in more common macroscopic systems. The optical collective excitation of atomic ensembles has led to the dramatic demonstration of macroscopic entanglement in free space.<sup>1-5</sup> Multilevel systems play a key role in these experiments, whether entanglement relies on off-resonant excitation induced Faraday rotation<sup>1-3</sup> or on spontaneous Raman scattering.<sup>4,5</sup> Several groups have been pursuing the ambitious objective of storing optically carried quantum information into an atomic ensemble entangled state and then returning quantum data to the optical carrier. Entanglement destruction by spontaneous emission can be avoided in a three-level system where the two lower states are connected by allowed optical transitions to a common upper state. By adequate coherent combination of the two resonantly excited optical transitions, the atomic Raman coherence could be combined with the radiation in a single quantum state. This fully quantum “dark polariton” scheme<sup>6</sup> is connected to processes such as “dark resonance,”<sup>7</sup> electromagnetically induced transparency (EIT),<sup>8</sup> “slow light,”<sup>9</sup> and stimulated Raman adiabatic passage (STIRAP).<sup>10</sup>

So far, ensemble entanglement has been demonstrated only in atomic vapors<sup>3,4</sup> and beams<sup>2</sup> or in laser cooled atom clouds.<sup>1,5</sup> However, rare-earth ion doped crystals (REIC) also

appear as promising candidates in the quest for macroscopic quantum effects. They offer properties similar to atomic vapors with the advantage of no atomic diffusion. Hyperfine levels of rare-earth ions are commonly used to perform coherent spectroscopy experiments, such as hole burning and photon echo.<sup>11</sup> At low temperature ( $< 4$  K) the optical coherence lifetime may reach several milliseconds in these materials and a hyperfine coherence lifetime of 82 ms has been reported in  $\text{Pr}^{3+}:\text{Y}_2\text{SiO}_5$ .<sup>12</sup> Given the absence of atomic motion, extremely long population lifetime can be observed. Notable experiments on systems in REIC include the demonstration of efficient EIT (Ref. 13) and phase conjugation,<sup>14</sup> and the observation of “slow light.”<sup>15</sup>

However, further investigation of hyperfine  $\Lambda$  systems in REIC is hampered by two main problems: (i) the  $\Delta M_I = 0$  selection rule where  $M_I$  is the nuclear-spin projection and (ii) the lack of adequate laser sources in the spectral range of the most attractive rare-earth ions.

Figure 1 represents a typical three-level  $\Lambda$  system.  $\Omega_1$  and  $\Omega_2$  are the Rabi frequencies which characterize the atom-laser interaction and are defined by

$$\Omega_1 = \frac{\mu_{13}\xi_1}{\hbar},$$

$$\Omega_2 = \frac{\mu_{23}\xi_2}{\hbar},$$

where  $\mu_{ij}$  is the electric dipole moment matrix element between states  $|i\rangle$  and  $|j\rangle$  and  $\xi_k$  is the field amplitude of laser  $k$ .

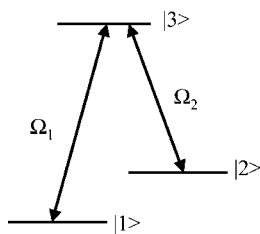


FIG. 1. Three-level  $\Lambda$  system coupled by two lasers.  $\Omega_1$  and  $\Omega_2$  are the Rabi frequencies which characterize the atom-laser interaction.

The possibility to control the relative strengths of the transitions, i.e., the Rabi frequencies, is very attractive for an efficient manipulation of this system. This can be performed by changing the field amplitude or by controlling the transition probabilities, i.e., the selection rule on the  $|1\rangle \rightarrow |3\rangle \rightarrow |3\rangle$  and  $|2\rangle \rightarrow |3\rangle$  transitions. In the case of rare-earth ions, the  $|1\rangle \rightarrow |3\rangle$  and  $|2\rangle \rightarrow |3\rangle$  transition strengths between hyperfine levels are usually very different due to the nuclear-spin selection rules. The aim of this paper is to show that by applying an external magnetic field which induces different  $M_I$  mixing in the ground ( $|1\rangle$ ,  $|2\rangle$ ) and excited ( $|3\rangle$ ) states, it is possible to relax the  $\Delta M_I$  selection rule and then to control the relative strengths of the  $|1\rangle \rightarrow |3\rangle$  and  $|2\rangle \rightarrow |3\rangle$  optical transitions.

Among all the rare-earth ions, non-Kramers ions with an even number of  $4f$  electrons present the longest coherence lifetime.<sup>16</sup> With the additional condition of a hyperfine structure of a few tens of megahertz splitting in the electronic ground state, one is practically left only with  $\text{Eu}^{3+}$ ,  $\text{Pr}^{3+}$ , and  $\text{Tm}^{3+}$  as good rare-earth ion candidates.

$\text{Eu}^{3+}$  and  $\text{Pr}^{3+}$  present a hyperfine structure at zero magnetic field due to the magnetic quadrupole and the second-order hyperfine interactions. In this case, state mixing may relax the selection rules to some extent in low symmetry compounds such as  $\text{Pr}^{3+}:\text{Y}_2\text{SiO}_5$  but in general the two transitions of the system may exhibit very different strengths. In a recent paper,<sup>17</sup> we showed that an appropriate external magnetic field can induce different hyperfine state mixing in the lower and upper electronic levels of the transition and thus relax the nuclear-spin selection rule in  $\text{Pr}^{3+}:\text{LiYF}_4$ . Therefore two parameters of importance in the context of coherent driving and quantum information physics, namely, the Rabi frequency and the sample optical density, both depending on the transition strength, can be controlled by the mean of the external magnetic field. Unfortunately, only dye lasers are available at the corresponding excitation wavelengths (580 nm for  $\text{Eu}^{3+}$  and 606 nm for  $\text{Pr}^{3+}$ ). Because of the high-frequency noise generated by the dye jet, this is a challenging task to reach the subkilohertz linewidth and jitter that are needed to match the long coherence time offered by REIC. Actually few dye laser systems throughout the world offer such a high degree of stability.<sup>18-20</sup>

In the absence of hyperfine structure at zero magnetic field, the lifting of nuclear-spin degeneracy under an applied magnetic field may offer an alternative way of building a system in REIC.<sup>21</sup> Among REIC devoid of hyperfine structure at zero field but offering more appropriate operation

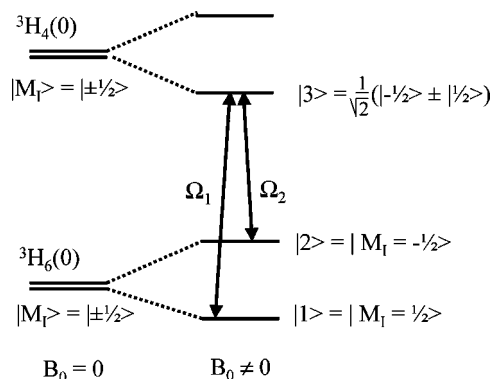


FIG. 2. Ideal three-level  $\Lambda$  system in the case of  $\text{Tm}^{3+}$  ions between three hyperfine levels of the first crystal-field states of the  ${}^3H_6(0)$  and  ${}^3H_4(0)$  multiplets. The external magnetic field  $B_0$  can induce different  $M_I$  mixing in the ground and excited states.

wavelength,  $\text{Tm}^{3+}$  in  $\text{Y}_3\text{Al}_5\text{O}_{12}$  (YAG) has been widely studied in the field of coherent transient-based signal-processing schemes.<sup>22,23</sup> The atomic coherence associated with the  ${}^3H_6(0) \rightarrow {}^3H_4(0)$  transition at 793 nm exhibits a lifetime of 70  $\mu\text{s}$  which grows to 150  $\mu\text{s}$  under moderate magnetic field.<sup>24</sup> What makes this compound attractive is that the  ${}^3H_6(0) \rightarrow {}^3H_4(0)$  transition falls in the spectral range of semiconductor lasers. Such lasers can be stabilized easily to subkilohertz linewidth and jitter.<sup>25</sup> The single natural isotope of thulium ( ${}^{169}\text{Tm}$ ) possesses a nuclear spin  $I=1/2$ . Application of an external magnetic field removes the nuclear-spin degeneracy and splits the electronic levels. A three-level  $\Lambda$  system with  $\text{Tm}^{3+}$  (Fig. 2) would involve the two hyperfine levels of the ground state  ${}^3H_6(0)$  and one hyperfine level of the excited state  ${}^3H_4(0)$ . At first sight, if  $M_I$  is a good quantum number, such a scheme seems to be doomed to failure because electronic excitation cannot flip the nuclear spin. Therefore, the two optical transitions that start from the two ground state sublevels seem to be unable to share a common upper level. However, in this work, we show that the coupling effect of the Zeeman electronic and the hyperfine interactions mixes the nuclear-spin states, which results in allowed transitions between the different hyperfine levels, making the  $\Lambda$  system effective. Carefully oriented applied magnetic field can lead to comparable oscillator strength values from both ground-state sublevels to a common upper level. The ideal situation is illustrated in Fig. 2 where the external magnetic field induces no  $M_I$  mixing in the ground state and a maximum  $M_I$  mixing in the excited state. In this case, the selection rule is released and the transition strengths of the  $|1\rangle = |1/2\rangle \rightarrow |3\rangle = \frac{1}{\sqrt{2}}(|-1/2\rangle \pm |1/2\rangle)$  and  $|3\rangle \rightarrow |2\rangle = |-1/2\rangle$  transitions are equal.

In order to relax the selection rules and to calculate the branching ratio between the two optical transitions, it is necessary to determine the hyperfine level wave functions for an arbitrary magnetic-field strength and direction. In this paper, we have performed wave-function calculations on  $\text{Tm}:\text{YAG}$  by taking into account all possible magnetic interactions. Two methods are used to describe the magnetic interactions: (i) a complete calculation starting from the crystal-field wave functions; such an approach has been successfully applied to

$\text{Pr}^{3+}$  in  $\text{CaF}_2$  (Refs. 26 and 27) and in  $\text{CsCdBr}_3$  (Ref. 28) and (ii) a spin-Hamiltonian approach which will be used to interpret the results of the previous calculations.

The paper is arranged as follows. In Sec. II, we present the crystal-field Hamiltonian approach and the complete calculation of the magnetic interactions from the crystal-field wave functions. The results are discussed in the case of Tm:YAG by analyzing the influence of the magnetic interactions on the  $M_l$  mixing. In Sec. III, we present and discuss the spin-Hamiltonian formalism which allows a physical and an analytical interpretation of the Tm:YAG calculations. In Sec. IV, an experimental protocol that makes a crystal similar to the atomic samples used in previous quantum information investigations, with the additional benefits of absence of motion and long coherence time, is described in the thulium doped YAG.

## II. COMPLETE CALCULATIONS FROM CRYSTAL-FIELD WAVE FUNCTIONS

### A. Theoretical description

Level and wave function calculations are performed using the complete Hamiltonian (CH) given by

$$H_{CH} = H_{FI} + H_{CF} + H_{EZ} + H_{HF} + H_{NZ} + H_Q, \quad (1)$$

where  $H_{FI}$  is the free-ion Hamiltonian,  $H_{CF}$  is the crystal-field one,  $H_{EZ}$  and  $H_{NZ}$  represent, respectively, the electronic and nuclear Zeeman interactions, and  $H_{HF}$  is the hyperfine Hamiltonian.  $H_Q$  is the electric quadrupole interaction which is nonzero for ions with nuclear spin  $I \geq 1$ . The free-ion interactions are written according to the formalism of Carnall *et al.*<sup>29</sup>

$$H_{FI} = H_0 + \sum_{k=1,2,3} E^k e_k + \zeta_{4f} A_{SO} + \alpha L(L+1) + \beta G(G_2) + \gamma G(R_7) + \sum_{i=2,3,4,6,7,8} t_i T^i. \quad (2)$$

In this expression,  $H_0$  is the spherical symmetric one-electron part of the Hamiltonian,  $E^k$  are the Racah parameters, and  $\zeta_{4f}$  is the spin-orbit coupling constant.  $e_k$  and  $A_{SO}$  represent the angular parts of the electrostatic repulsion and the spin-orbit coupling, respectively.  $\alpha$ ,  $\beta$ , and  $\gamma$  are associated with the two-body interactions and the  $T^i$  (Judd parameters) with the three-body interactions.  $G(G_2)$  and  $G(R_7)$  are the eigenvalues of Casimir's operators for the groups  $G_2$  and  $R_7$ .<sup>30</sup> The Judd parameters are vanishing for the  $f^2$  and  $f^{12}$  configurations. Other interactions such as spin-spin and spin-other orbit interactions, operating through  $M^k$  and  $P^k$  parameters, are not included in the calculations. Following the Wybourne's formalism,<sup>30</sup> the crystal-field Hamiltonian is expressed as a sum of products of crystal-field parameters and spherical harmonics  $Y_{kq}$ :

$$H_{CF} = \sum_{k=2}^{4,6} \sum_{q=0}^k \{B_q^k [C_q^{(k)} + (-1)^q C_{-q}^{(k)}] + iS_q^k [C_q^{(k)} - (-1)^q C_{-q}^{(k)}]\} \quad (3)$$

with

$$C_q^{(k)} = \sqrt{\frac{4\pi}{2k+1}} Y_{kq}. \quad (4)$$

The number of nonzero crystal-field parameters  $B_q^k$  and  $S_q^k$ , real and imaginary parts, depends on the site symmetry of the lanthanide ion in the structure.

The electronic Zeeman interaction between the  $n$  electrons of the  $4f^n$  configuration and the external magnetic field  $\mathbf{B}_0$  is written as<sup>30</sup>

$$H_{EZ} = \beta \mathbf{B}_0 \cdot \sum_{i=1}^n (\mathbf{l}_i + g_s \mathbf{s}_i) = \beta \mathbf{B}_0 \cdot (\mathbf{L} + g_s \mathbf{S}), \quad (5)$$

where  $\beta$  is the electronic Bohr magneton,  $\mathbf{l}_i$  and  $\mathbf{s}_i$  are the individual orbital and spin momenta of the electrons,  $\mathbf{L} = \sum_{i=1}^n \mathbf{l}_i$ , and  $\mathbf{S} = \sum_{i=1}^n \mathbf{s}_i$ .  $g_s$  is the gyromagnetic ratio of the electron spin which is slightly larger than 2. The hyperfine Hamiltonian  $H_{HF}$  which results from the interaction between the nuclear spin and the magnetic field at the nucleus produced by the  $4f$  electron is<sup>31</sup>

$$H_{HF} = g_s \beta \beta_n g_n \sum_{i=1}^n \frac{\mathbf{N}_i \cdot \mathbf{I}}{r_i^3} \quad (6)$$

where

$$\mathbf{N}_i = \mathbf{l}_i - \mathbf{s}_i + 3\mathbf{r}_i(\mathbf{s}_i \cdot \mathbf{r}_i)/r_i^2,$$

$\beta_n$  is the nuclear magneton, and  $g_n$  is the nuclear  $g$  factor.  $\mathbf{r}_i$  is the radius of the electron orbital and  $\mathbf{I}$  is the nuclear-spin operator.

The nuclear Zeeman interaction between the nuclear spin and the external magnetic field  $\mathbf{B}_0$  is written as,

$$H_{NZ} = -g_n \beta_n \mathbf{B}_0 \cdot \mathbf{I}. \quad (7)$$

The electric quadrupole interaction  $H_Q$  for nuclei with spin  $I \geq 1$  which results from the interaction between the nuclear quadrupole momentum and the electron momentum is given by<sup>30</sup>

$$H_Q = -e^2 \int \int \frac{\rho_e(r_e) \rho_n(r_n)}{|r_e - r_n|} d\tau_e d\tau_n, \quad (8)$$

where  $-\rho_e(r_e)$  and  $e\rho_n(r_n)$  are the electron and nuclear charge densities, respectively.  $r_e$  and  $r_n$  are taken relative to the center of the nucleus.

All the previous Hamiltonians are calculated and diagonalized in the  $|\gamma LSJM_J IM_I\rangle$  basis set where  $\gamma$  stands for  $|f^n \tau WU\rangle$ . The  $\tau WU$  quantum numbers are used to unambiguously describe each state of the electronic configuration. For a more detailed definition of these quantum numbers see Ref. 30 or 31. The matrix elements of the magnetic interactions in the  $|\gamma LSJM_J IM_I\rangle$  basis set that we use in the present work are given in the Appendix. Indeed, it seemed to us difficult to find in the literature suitable expressions for those matrix elements as notations, and equations can vary from author to author.

### B. Results and discussion

In the case of Tm:YAG crystal, the complete calculation is performed in two steps. First, the energy levels, deter-

TABLE I. Free-ion and crystal-field parameters for  $\text{Tm}^{3+}$  ions in YAG single crystals (in  $\text{cm}^{-1}$ ) and experimental and calculated energy levels (in  $\text{cm}^{-1}$ ) corresponding to the two  ${}^3H_6$  and  ${}^3H_4$  multiplets of interest in this work. The parameter within square brackets is kept constant during adjustment. The number after the parameters represent the uncertainties. The rms standard deviation  $\sigma$  is indicated.

Parameters ( $\text{cm}^{-1}$ )	Multiplet ${}^{2S+1}L_J$	Energy levels ( $\text{cm}^{-1}$ )		
		Experimental	Calculated	
$E^0$	17 443 (1)	${}^3H_6$	0	0
$E^1$	7018 (2)		27	26
$E^2$	33.38 (0.02)		216	237
$E^3$	671.5 (0.1)		240	246
$\alpha$	17.06 (0.06)		247	260
$\beta$	-658 (7)		300	314
$\gamma$	[0]		450	473
$\zeta_{4f}$	2619.7 (0.9)		588	603
$B_0^2$	580 (12)		610	634
$B_0^4$	-59 (29)		650	653
$B_0^6$	-1223 (36)		690	699
$B_2^2$	29 (9)		730	780
$B_2^4$	-1403 (16)			798
$B_4^4$	-716(19)			
$B_2^6$	-331 (22)			
$B_4^6$	460 (28)	${}^3H_4$	12607	12607
$B_6^6$	-369 (22)		12644	12669
$\sigma$	20.8		12732	12744
			12747	12768
			12824	12857
				13001
			13036	13062
			13112	13127
			13152	13165

mined by Tiseanu *et al.*<sup>32</sup> from absorption and emission measurements, are used to calculate the parameters of the free-ion and crystal-field Hamiltonian.

For the free-ion Hamiltonian, eight parameters were varied, i.e.,  $E^0$ ,  $E^1$ ,  $E^2$ , and  $E^3$  (Racah parameters);  $\alpha$ ,  $\beta$ , and  $\gamma$  (Trees parameters), and  $\zeta_{4f}$ .  $\text{Tm}^{3+}$  substitutes  $\text{Y}^{3+}$  in YAG in a  $D_2$  point site symmetry. The  $D_2$  crystal-field parameters involve nine nonzero real  $B_q^k$  crystal-field parameters, namely,  $B_0^2$ ,  $B_0^4$ ,  $B_0^6$ ,  $B_2^2$ ,  $B_2^4$ ,  $B_2^6$ ,  $B_4^4$ ,  $B_4^6$ , and  $B_6^6$ . The simulation of the energy-level scheme is performed on 71 experimental levels among the 91 possible levels of the  $4f^{12}$  configuration. We did not take into account the free-ion parameters of Tiseanu *et al.* because in their work the barycenters of each multiplet  ${}^{2S+1}L_J$  are adjustable parameters which means that they were not fitted to the experimental levels. With a starting set of phenomenological free-ion and crystal-field parameters taken from the work of Gruber *et al.*,<sup>33</sup> the rms standard deviation  $\sigma$ , taken as the figure of merit for the simulation, decreases to a rather good final value of  $20.8 \text{ cm}^{-1}$ . Table I

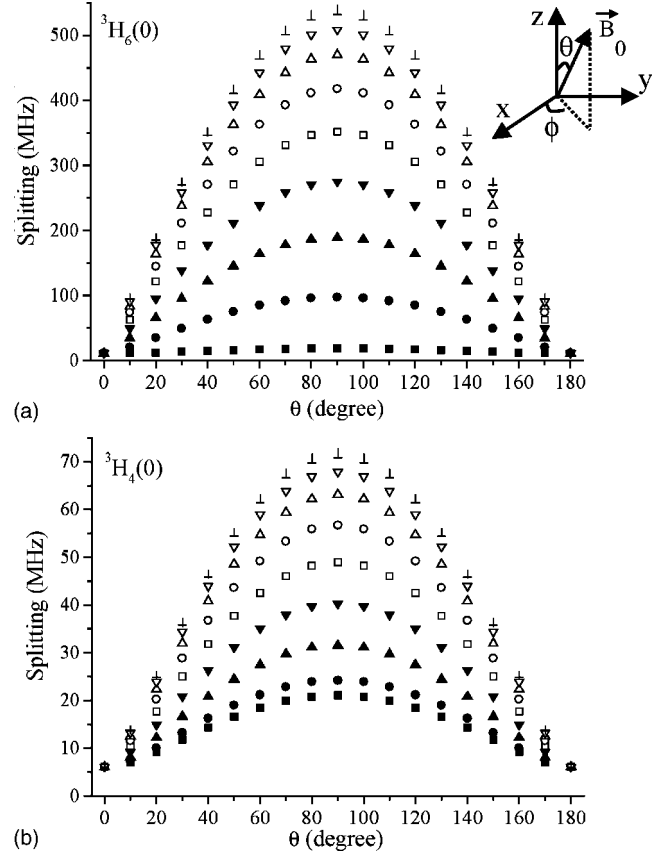


FIG. 3. Hyperfine splittings (in megahertz) of the (a)  ${}^3H_6(0)$  and (b)  ${}^3H_4(0)$  states of  $\text{Tm}:\text{YAG}$  as a function of the external magnetic-field direction and for  $|\mathbf{B}_0|=1 \text{ T}$ . (■)  $\phi=0^\circ$ , (●)  $\phi=10^\circ$ , (▲)  $\phi=20^\circ$ , (▼)  $\phi=30^\circ$ , (□)  $\phi=40^\circ$ , (○)  $\phi=50^\circ$ , (△)  $\phi=60^\circ$ , (▽)  $\phi=70^\circ$ , (◇)  $\phi=80^\circ$ , and (◊)  $\phi=90^\circ$ . ( $x, y, z$ ) refers to the local crystal-field axes.

gathers the free-ion and crystal-field parameters for  $\text{Tm}^{3+}$  ions in YAG single crystals and experimental and calculated energy levels of the two  ${}^3H_6$  and  ${}^3H_4$  multiplets. The rms standard deviation is given for the 71 experimental levels. In the simulation, the  $\gamma$  parameter is fixed to zero as it does not seem to influence the calculated energy levels. The crystal-field Hamiltonian ( $H_{CF}$ ) leaves each electronic level as a nondegenerate singlet due to the low point site symmetry of  $\text{Tm}^{3+}$  ions in the YAG host.

The second step of the calculation starts with the previous free-ion and crystal-field parameters by including in the complete secular determinant the electronic Zeeman, the hyperfine, and the nuclear Zeeman interactions. Without any external magnetic field, each electronic singlet is composed of two degenerate hyperfine levels due to the two  $M_I = \pm \frac{1}{2}$  nuclear-spin projections associated to the nuclear spin of the  $\text{Tm}^{3+}$  ion. The complete diagonalization is performed on a  $182 \times 182$  matrix. The magnetic interactions are computed using a  $4f$  radial extensions of  $\langle r^{-3} \rangle_{4f} = 13.6 \text{ a.u.}$ <sup>30</sup> (see the Appendix for the matrix elements). Figure 3 gathers the calculated splittings (in megahertz) between the hyperfine levels of the  ${}^3H_6(0)$  and the  ${}^3H_4(0)$  states as a function of the external magnetic-field direction and for  $|\mathbf{B}_0|=1 \text{ T}$ . It is important to note that in the following discussion, the orientation

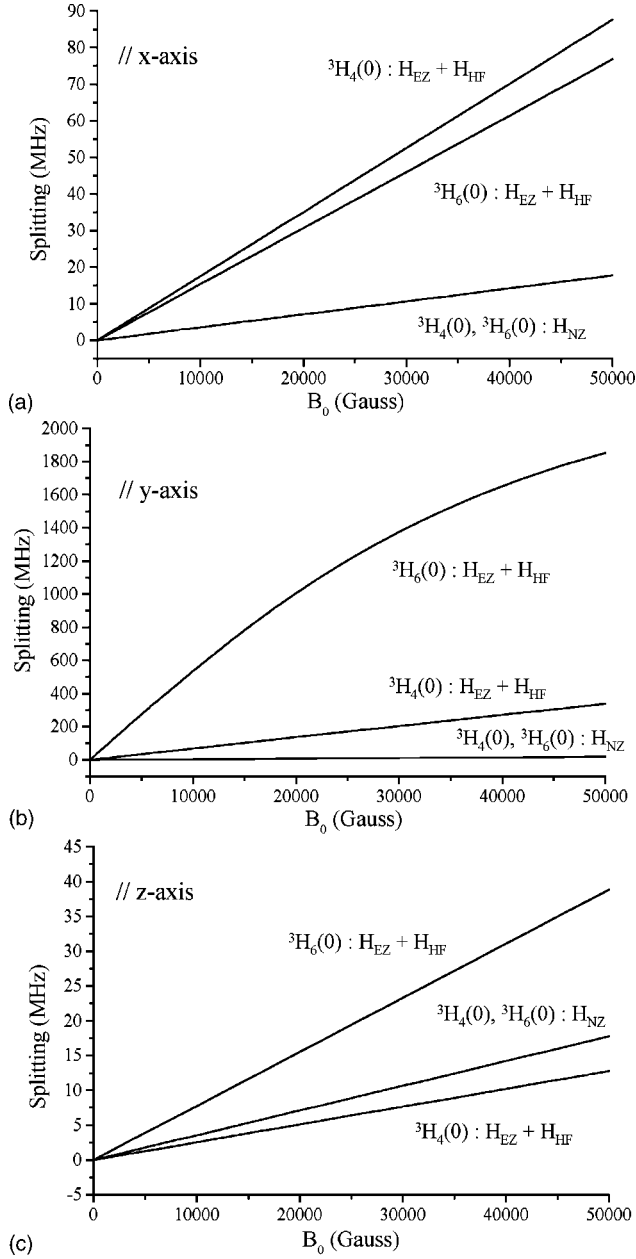


FIG. 4. Contributions of the nuclear Zeeman interaction ( $H_{EZ}$ ) and of the coupling of the electronic Zeeman and hyperfine interactions ( $H_{NZ}+H_{HF}$ ) to the hyperfine splittings of the  ${}^3H_6(0)$  and the  ${}^3H_4(0)$  states in Tm:YAG as a function of  $\mathbf{B}_0$  intensity. The calculations are performed for three different orientations of the magnetic field parallel to the  $x$ ,  $y$ , and  $z$  axes.

of the applied magnetic field is expressed in the local  $(x, y, z)$  crystal-field axes. The splitting is strongly dependent on the orientation of the external magnetic field. For the same orientation of  $\mathbf{B}_0$ , the two crystal-field levels are characterized by different hyperfine splittings [Figs. 3(a) and 3(b)]. They are stronger for the ground state  ${}^3H_6(0)$  than for the excited state  ${}^3H_4(0)$ .

The nuclear Zeeman interaction lifts the nuclear degeneracy of each electronic crystal-field level into two hyperfine levels. From time inversion symmetry property,<sup>34</sup> the electronic Zeeman and the hyperfine interactions at first order

have no effect on the energy levels as they do not split the  $M_I$  degeneracy. It is the coupling of these interactions to second order which provides an additional hyperfine splitting. To compare the order of magnitude of each magnetic contribution, we have performed two kinds of calculations for three different orientations of the external magnetic field (along the  $x$ ,  $y$ , and  $z$  axes): (i) calculation by considering only the nuclear Zeeman interaction and (ii) calculation by taking into account only the electronic Zeeman and the hyperfine interactions (Fig. 4). If we consider only the nuclear Zeeman interaction, the hyperfine splittings of both crystal-field levels [ ${}^3H_6(0)$  and  ${}^3H_4(0)$ ] are identical as they are characterized by a single nuclear  $g_n$  value. For each crystal-field level, the coupling of  $H_{EZ}$  and  $H_{HF}$  can be of the same order of magnitude or even higher than the nuclear Zeeman interaction. The  $\{H_{EZ}+H_{HF}\}$  Hamiltonian is stronger for the  ${}^3H_6(0)$  level than for the  ${}^3H_4(0)$  level (Fig. 4). This explains that the hyperfine splitting is higher in the ground state than in the excited state. These different hyperfine splittings could allow one to obtain for a given magnetic-field orientation a different  $M_I$  mixing in the  ${}^3H_6(0)$  and  ${}^3H_4(0)$  levels. It could be then possible to release the selection rules on the nuclear-spin projections and therefore to obtain an efficient three-level  $\Lambda$  system.

A way to represent the  $M_I$  mixing is to associate to each crystal-field level an effective magnetic field  $\mathbf{B}^{eff}$  whose intensity  $B^{eff}$  is proportional to the hyperfine splitting and whose orientation ( $\theta^{eff}$  and  $\phi^{eff}$  in polar coordinates) is directly linked to the coefficients of the nuclear part of the wave function. The determination of such effective magnetic field is possible if we can separate the nuclear part of the wave function from its electronic part. For each orientation of  $\mathbf{B}_0$ , this behavior has been checked by analyzing the whole crystal-field wave functions which can then be written in the  $2 \times 2$  hyperfine subspace ( $M_I = \pm \frac{1}{2}$ ) as

$$|\Psi_{\pm}\rangle = |\Psi_{\pm}^{nucl}\rangle |\Psi_{elec}\rangle \quad (9)$$

with

$$|\Psi_{\pm}^{nucl}\rangle = a_{\pm} |M_I = +\frac{1}{2}\rangle + b_{\pm} |M_I = -\frac{1}{2}\rangle \quad (10)$$

and  $|\Psi_{elec}\rangle$  is the electronic part of the wave function. The orthogonality condition  $a_{+}^* a_{+} + b_{+}^* b_{+} = 0$  is fulfilled. The polar coordinates of the effective magnetic field  $\mathbf{B}^{eff}$  ( $B^{eff}$ ,  $\theta^{eff}$ ,  $\phi^{eff}$ ) are determined by considering that  $|\Psi_{\pm}^{nucl}\rangle$  are eigenvalues of the following effective nuclear Zeeman Hamiltonian:

$$H^{eff} = -g_n \beta \mathbf{B}^{eff} \cdot \mathbf{I} = -g_n \beta (B_x^{eff} I_x + B_y^{eff} I_y + B_z^{eff} I_z) \quad (11)$$

with

$$H^{eff} |\Psi_{\pm}^{nucl}\rangle = \mp \frac{1}{2} E |\Psi_{\pm}^{nucl}\rangle, \quad (12)$$

where  $E$  is the hyperfine splitting. From Eqs. (11) and (12), we obtain

$$-g_n \beta B^{eff} [b_{\pm} e^{-i\phi^{eff}} \sin \theta^{eff} + a_{\pm} \cos \theta^{eff}] = \mp E a_{\pm},$$

$$-g_n \beta B^{eff} [a_{\pm} e^{+i\phi^{eff}} \sin \theta^{eff} - b_{\pm} \cos \theta^{eff}] = \mp E b_{\pm},$$

and then by writing

$$a_{\pm} = \cos \frac{\theta^{eff}}{2}, \quad (13)$$

$$b_{\pm} = e^{i\phi^{eff}} \sin \frac{\theta^{eff}}{2},$$

we have

$$E = g_n \beta B^{eff}. \quad (14)$$

The orientations  $\theta^{eff}$  and  $\phi^{eff}$  of the effective magnetic field are linked to the coefficients  $a_{\pm}$  and  $b_{\pm}$  of  $|\Psi_{\pm}^{nucl}\rangle$  [Eq. (13)], and the hyperfine splitting  $E$  gives the intensity of the effective magnetic field  $B^{eff}$  [Eq. (14)]. For example, an effective magnetic field along the quantification  $z$  axis ( $\theta^{eff} = 0^\circ$  and  $\phi^{eff} = 0^\circ$ ) gives two pure  $M_I$  states  $|\Psi_{\pm}^{nucl}\rangle = |M_I = \pm \frac{1}{2}\rangle$ . An effective magnetic field along the  $x$  axis, ( $\theta^{eff} = 90^\circ$  and  $\phi^{eff} = 0^\circ$ ) leads to a maximum  $M_I$  mixing:  $|\Psi_{\pm}^{nucl}\rangle = (1/\sqrt{2})(|M_I = +\frac{1}{2}\rangle \pm |M_I = -\frac{1}{2}\rangle)$ . To reach the ideal case of Fig. 2, we have then to find an orientation of  $\mathbf{B}_0$  for which the two effective magnetic fields  $B_g^{eff}$  and  $B_e^{eff}$  associated to the ground  ${}^3H_6(0)$  and the excited  ${}^3H_4(0)$  levels, respectively, are perpendicular. In the following, we note  $\alpha^{eff}$ , the angle between these two effective fields, and we define, by considering the nuclear part of the wave functions, the transition strength ratio  $R$  between the  $|2\rangle \rightarrow |3\rangle$  and  $|1\rangle \rightarrow |3\rangle$  transitions as

$$R = \frac{|\langle 2|3\rangle_{nucl}|^2}{|\langle 1|3\rangle_{nucl}|^2}. \quad (15)$$

The ideal situation of Fig. 2 is obtained when  $R=1$ .

Figure 5 gathers the angle  $\alpha^{eff}$  between the two effective magnetic fields and the transition strength ratio  $R$  between the hyperfine levels of the  ${}^3H_6(0)$  and  ${}^3H_4(0)$  states as a function of the orientation of the external magnetic field  $\mathbf{B}_0$  in the local crystal-field axes. In Tm:YAG, the ideal case of Fig. 2, corresponding to  $\alpha^{eff} = 90^\circ$  and  $R=1$ , cannot be reached whatever is the orientation of  $\mathbf{B}_0$  (Fig. 5). A maximum value of  $\alpha^{eff} = 52^\circ$  is found for  $\mathbf{B}_0$  in the  $x$ - $y$  plane with  $\theta = 90^\circ$  and  $\phi = 6^\circ$  [Fig. 5(a)]. This maximum angle between the two effective magnetic fields corresponds to  $R=0.24$  [Fig. 5(b)]. This gives a transition strength ratio around 1:4 for the  $|2\rangle \rightarrow |3\rangle$  and  $|1\rangle \rightarrow |3\rangle$  transitions. The maximum value of  $R$  that we can reach in Tm:YAG is not the ideal case of Fig. 2 but still provides a good three-level  $\Lambda$  system.  $\alpha^{eff}$  and  $R$  are very sensitive to  $\phi$  around  $\phi = 6^\circ$  as shown in Fig. 6 and have a smoother dependence on  $\theta$  around  $\theta = 90^\circ$  (Fig. 7). This behavior implies that in a real experiment, we have to accurately control the external magnetic-field orientation.

### III. SPIN-HAMILTONIAN APPROACH

#### A. Theoretical description

Another way to express the different magnetic interactions is to use a spin-Hamiltonian (SH) formalism which is based on the equivalent operator method.<sup>34</sup> The spin-Hamiltonian formalism is very useful to understand the previous results as it allows an analytical description of the

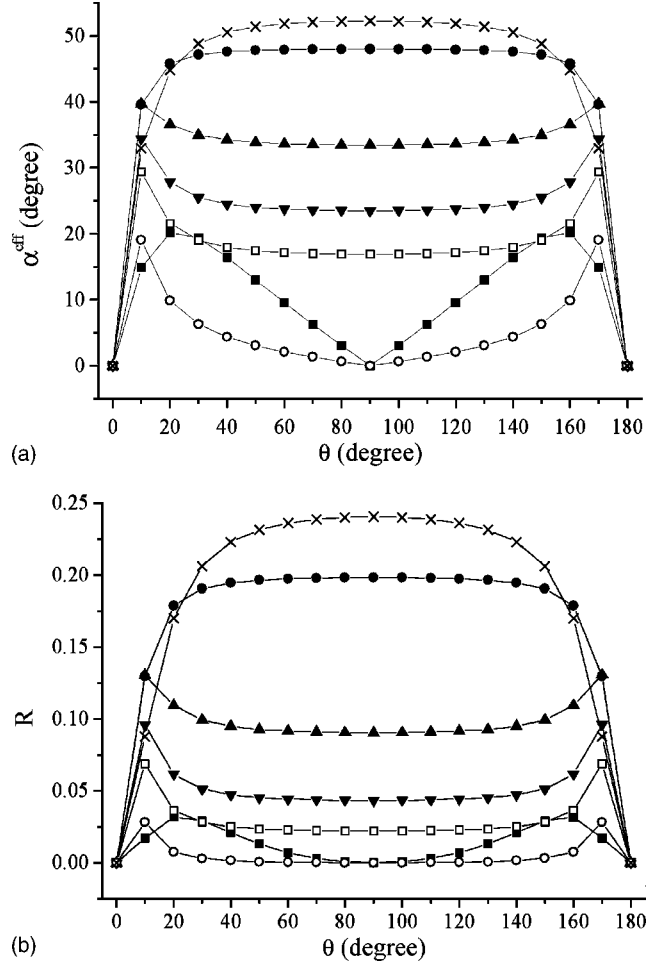


FIG. 5. (a) Angle  $\alpha^{eff}$  in degree between the two effective magnetic fields and (b) transition strength ratio  $R$  associated to the hyperfine levels of the  ${}^3H_6(0)$  and  ${}^3H_4(0)$  states as a function of the angle  $\theta$  of the magnetic field  $\mathbf{B}_0$  ( $|\mathbf{B}_0|=1$  T). ( $\blacksquare$ )  $\phi=0^\circ$ , ( $\times$ )  $\phi=6^\circ$ , ( $\bullet$ )  $\phi=10^\circ$ , ( $\blacktriangle$ )  $\phi=20^\circ$ , ( $\blacktriangledown$ )  $\phi=30^\circ$ , ( $\square$ )  $\phi=40^\circ$ , and ( $\circ$ )  $\phi=90^\circ$ . The lines are guide to eyes. The angles are given in the local crystal-field axes.

complex crystal-field calculations. This method consists in the neglect of all the  $J$ -mixing effects (due to second-order effects of the crystal-field Hamiltonian) and in only the consideration of the diagonal term in  $J$ . In this way, the magnetic interactions can be analyzed by the following spin Hamiltonian in the case of a non-Kramers ion in low site symmetry:<sup>35</sup>

$$H_{SH} = \sum_{i=x,y,z} \gamma_i \mathbf{B}_0 \cdot \mathbf{I} + D \left[ I_z^2 - \frac{1}{3} I(I+1) \right] + E (I_x^2 - I_y^2). \quad (16)$$

The parameters in  $H_{SH}$  are determined by first- and second-order perturbation theory and are calculated by taking into account all the crystal-field levels of a particular  $J$  multiplet. This means that each multiplet  $J$  is characterized by a set of  $\gamma_i$ ,  $D$ , and  $E$  values. The spin-Hamiltonian parameters are given by

$$D = D_a + P, \quad (17)$$

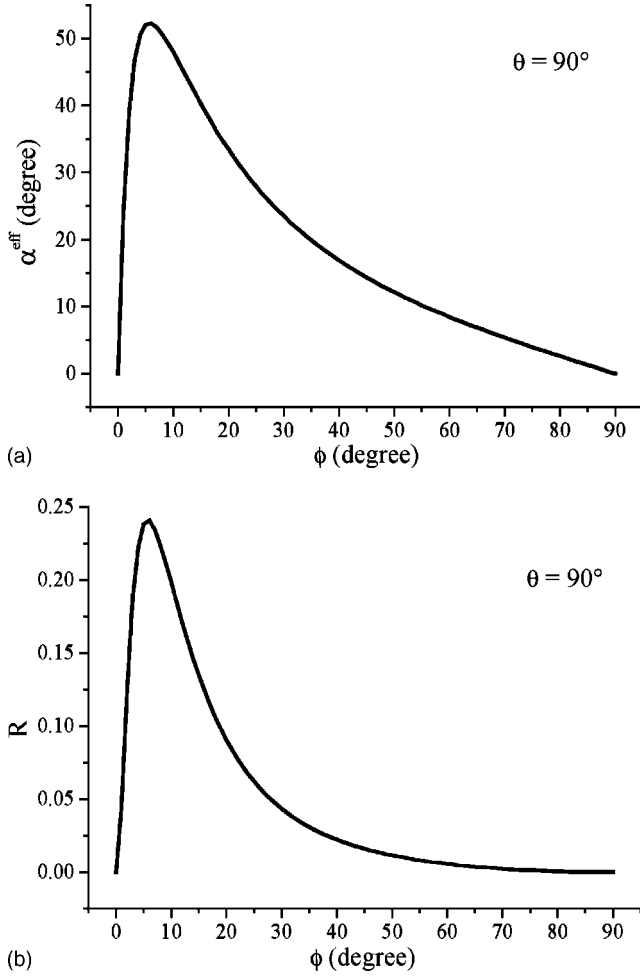


FIG. 6. (a) Angle  $\alpha^{eff}$  in degree between the two effective magnetic fields and (b) transition strengths ratio  $R$  associated to the hyperfine levels of the  ${}^3H_6(0)$  and  ${}^3H_4(0)$  states as a function of the angle  $\phi$  ( $|\mathbf{B}_0|=1$  T) for  $\theta=90^\circ$ . The angles are given in the local crystal-field axes.

$$E = E_a + \eta \frac{P}{3}, \quad (18)$$

$$D_a = A \left( \frac{\Lambda_{xx} + \Lambda_{yy}}{2} - \Lambda_{zz} \right), \quad (19)$$

$$E_a = A \frac{\Lambda_{yy} - \Lambda_{xx}}{2}, \quad (20)$$

where  $P$  is the quadrupole-coupling constant,  $\eta$  an asymmetry parameter, and  $A$  is the hyperfine interaction constant. The second-order parameters are

$$\gamma_i = -g_n \beta_n - 2g\beta \Lambda_{ii} \quad (21)$$

and

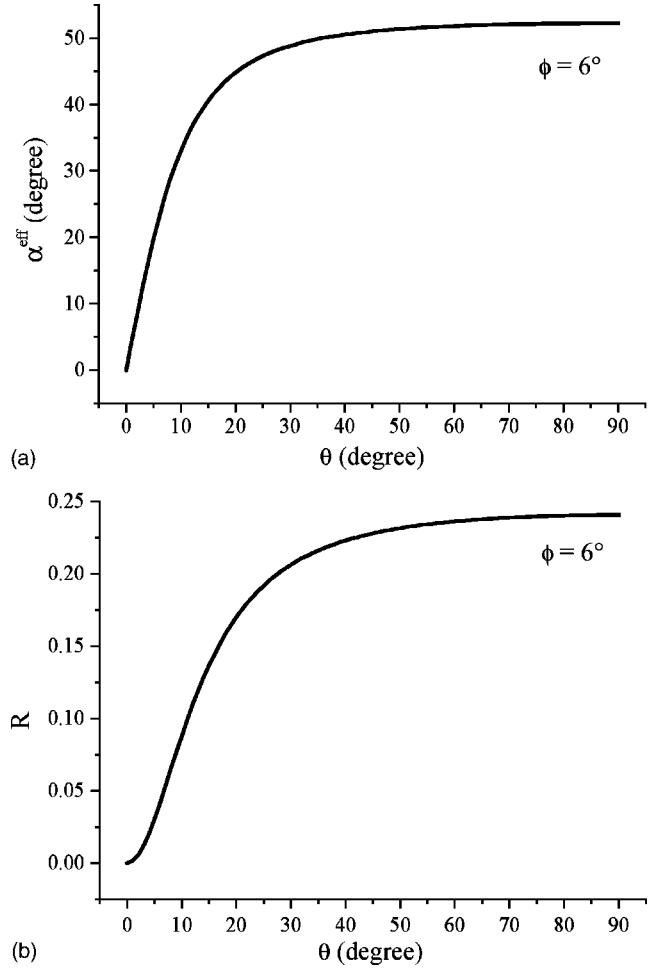


FIG. 7. (a) Angle  $\alpha^{eff}$  in degree between the two effective magnetic fields and (b) transition strength ratio  $R$  associated to the hyperfine levels of the  ${}^3H_6(0)$  and  ${}^3H_4(0)$  states as a function of the angle  $\theta$  ( $|\mathbf{B}_0|=1$  T) for  $\phi=6^\circ$ . The angles are given in the local crystal-field axes.

$$\Lambda_{ii} = \sum_{n \neq 0} A \frac{|\langle 0 | J_i | n \rangle|^2}{E_n - E_0}. \quad (22)$$

The index 0 denotes the first crystal-field level [ ${}^3H_6(0)$  or  ${}^3H_4(0)$ ] and  $n$  the other CF levels of a  ${}^{2S+1}L_J$  multiplet.  $E_n$  is the energy of the CF level  $n$ .

The different parameters of the spin Hamiltonian can be experimentally determined by optically detected NMR measurements.<sup>36,37</sup> In the following we use this approach to explain the different results of the complete calculations. The spin-Hamiltonian parameters are determined by using the crystal-field wave functions.

## B. Results and discussion

From the complete crystal-field calculation, we have seen that the coupling of the electronic Zeeman and of the hyperfine interactions bring an important contribution to the hyperfine splitting. This effect appears clearly in the spin-Hamiltonian formalism. Indeed, in Eq. (21), the  $\gamma_i$  factor is a sum of two terms: the first one  $g_n \beta_n$  which is due to the

TABLE II. Spin-Hamiltonian parameters of the first crystal-field states of the  ${}^3H_6$  and  ${}^3H_4$  multiplets.

Parameters	Crystal-field level	
	${}^3H_6(0)$	${}^3H_4(0)$
$g$	1.16	0.95
$A$ (MHz)	-470.3	-678.3
$\Lambda_{xx}$	$-4 \times 10^{-4}$	$-7 \times 10^{-4}$
$\Lambda_{yy}$	$-1.7 \times 10^{-2}$	$-2.7 \times 10^{-3}$
$\Lambda_{zz}$	$-2 \times 10^{-4}$	$-1 \times 10^{-4}$
$\gamma_x$ (kHz/G)	1.89	2.23
$\gamma_y$ (kHz/G)	55.96	7.52
$\gamma_z$ (kHz/G)	1.12	0.63

nuclear Zeeman interaction and the second one  $g\beta\Lambda_{ii}$  which is the product of the electronic Zeeman interaction  $g\beta$  and the hyperfine interaction  $\Lambda_{ii}$ . The second term is often called pseudonuclear Zeeman interaction.<sup>34</sup> As the hyperfine term  $\Lambda_{ii}$  is strongly dependent on the crystal-field splitting of the  $J$  multiplet [Eq. (22)], it is not surprising to obtain different hyperfine splittings for the ground state [ ${}^3H_6(0)$ ] and the excited state [ ${}^3H_4(0)$ ].

We will restrict the following discussion, which is general for ions with nuclear spin  $I=1/2$ , in the particular  $x$ - $y$  local plane. Indeed, it is possible for this orientation to obtain an analytical expression for the transition strength ratio  $R$ , and also it is in the  $x$ - $y$  plane that the complete calculation (Sec. II) gives the best three-level  $\Lambda$  system in Tm:YAG with a transition strength ratio  $R$  of 0.24. The spin-Hamiltonian for  $\text{Tm}^{3+}$  ions is

$$H_{SH} = \sum_{i=x,y,z} \gamma_i \mathbf{B}_0 \cdot \mathbf{I}, \quad (23)$$

which gives the following matrix elements in the  $\{|M_I = -\frac{1}{2}\rangle, |M_I = +\frac{1}{2}\rangle\}$  basis set:

$$H_{SH} = \frac{1}{2} \begin{pmatrix} -\gamma_z B_{0z} & \gamma_x B_{0x} + i\gamma_y B_{0y} \\ \gamma_x B_{0x} - i\gamma_y B_{0y} & \gamma_z B_{0z} \end{pmatrix} \quad (24)$$

with  $\mathbf{B}_0$  given in the local crystal-field axes. From the crystal-field calculations, the spin-Hamiltonian parameters have been calculated and are gathered in Table II for the  ${}^3H_6(0)$  and  ${}^3H_4(0)$  states.

When  $\gamma_x B_{0x} - i\gamma_y B_{0y} = 0$  ( $\mathbf{B}_0$  parallel to the  $z$  axis), the nuclear part of the wave functions of the  ${}^3H_6(0)$  and  ${}^3H_4(0)$  states are pure in  $M_I$ :  $|\Psi_{\pm}^{nuc}\rangle = |M_I = \pm \frac{1}{2}\rangle$ . The system is not an efficient three-level  $\Lambda$  system as the optical  $|2\rangle \rightarrow |3\rangle$  transition is forbidden ( $R=0$ ).

When  $\gamma_x B_{0x} - i\gamma_y B_{0y} \neq 0$  ( $\mathbf{B}_0$  in the  $x$ - $y$  plane) the eigenvalues and eigenvectors of  $H_{SH}$  are, respectively:

$$E_1 = -\frac{1}{2} \sqrt{\gamma_x^2 B_{0x}^2 + \gamma_y^2 B_{0y}^2 + \gamma_z^2 B_{0z}^2},$$

$$|1\rangle = p |M_I = -\frac{1}{2}\rangle + |M_I = +\frac{1}{2}\rangle, \quad (25)$$

$$E_2 = \frac{1}{2} \sqrt{\gamma_x^2 B_{0x}^2 + \gamma_y^2 B_{0y}^2 + \gamma_z^2 B_{0z}^2},$$

$$|2\rangle = |M_I = -\frac{1}{2}\rangle - p^* |M_I = +\frac{1}{2}\rangle, \quad (26)$$

with

$$p = \frac{E_1 - \frac{\gamma_z B_{0z}}{2}}{\frac{\gamma_x B_{0x} - i\gamma_y B_{0y}}{2}}. \quad (27)$$

The above wave functions are not normalized as it does not influence the following discussion.

In the  $x$ - $y$  plane, Eq. (27) gives

$$p_{xy} = -\frac{\gamma_x B_{0x} + i\gamma_y B_{0y}}{\sqrt{\gamma_x^2 B_{0x}^2 + \gamma_y^2 B_{0y}^2}} = e^{i\delta} \quad (28)$$

with

$$\cos \delta = -\frac{\gamma_x B_{0x}}{\sqrt{\gamma_x^2 B_{0x}^2 + \gamma_y^2 B_{0y}^2}}, \quad (29)$$

$$\sin \delta = -\frac{\gamma_y B_{0y}}{\sqrt{\gamma_x^2 B_{0x}^2 + \gamma_y^2 B_{0y}^2}}. \quad (30)$$

In this plane, the transition strength ratio  $R_{xy}$  is

$$R_{xy} = \frac{|p^e - p^s|^2}{|(p^s)^* p^e + 1|^2} = \tan^2 \left( \frac{\delta^e - \delta^s}{2} \right), \quad (31)$$

where  $g$  ( $e$ ) means ground  ${}^3H_6(0)$  [excited  ${}^3H_4(0)$ ] state. The condition  $R_{xy}=1$  gives  $\delta^e - \delta^s = 90^\circ$ . A simple calculation shows that the difference  $\delta^e - \delta^s$  is exactly the angle  $\alpha^{eff}$  between the two effective magnetic fields. As  $\tan(\delta^e - \delta^s) = (\tan \delta^e - \tan \delta^s) / (1 + \tan \delta^e \tan \delta^s)$ , the condition  $\delta^e - \delta^s = 90^\circ$  gives  $\tan \delta^e \tan \delta^s = -1$  which is equivalent to  $[(\gamma_y^e / \gamma_x^e)(\gamma_y^s / \gamma_x^s)] (B_0^y / B_0^x)^2 = -1$ . When  $(\gamma_y^e / \gamma_x^e)(\gamma_y^s / \gamma_x^s)$  is positive, it is not possible to find in the  $x$ - $y$  plane  $R_{xy}=1$ . It is why in the case of Tm:YAG, as all the  $\gamma_i$  are positive (see Table II), we could not find a  $\mathbf{B}_0$  orientation giving the ideal case of Fig. 2. In this plane, when  $(\gamma_y^e / \gamma_x^e)(\gamma_y^s / \gamma_x^s)$  is positive, a maximum transition strength ratio  $R_{xy}^{\max}$  can be calculated by

$$R_{xy}^{\max} = \tan^2 \left[ \frac{1}{2} \arctan \left( \frac{\frac{\gamma_y^e}{\gamma_x^e} - \frac{\gamma_y^s}{\gamma_x^s}}{2 \sqrt{\frac{\gamma_y^e \gamma_y^s}{\gamma_x^e \gamma_x^s}}} \right) \right] \quad (32)$$

for a  $\mathbf{B}_0$  orientation of  $\theta=90^\circ$  and  $\phi = \arctan(1 / \sqrt{(\gamma_y^e / \gamma_x^e)(\gamma_y^s / \gamma_x^s)})$ .

Figure 8(a) plots  $R_{xy}^{\max}$  as a function of  $(\gamma_y^e / \gamma_x^e) / (\gamma_y^s / \gamma_x^s)$ . For small values of  $(\gamma_y^e / \gamma_x^e) / (\gamma_y^s / \gamma_x^s)$  (inferior to 0.2),  $R_{xy}^{\max}$  rapidly increases and  $R_{xy}^{\max} \rightarrow 1$  when  $(\gamma_y^e / \gamma_x^e) / (\gamma_y^s / \gamma_x^s) \rightarrow 0$ . The black circle in Fig. 8(a) represents the case of Tm:YAG. From the  $\gamma_i$  values of Table II,  $(\gamma_y^e / \gamma_x^e) / (\gamma_y^s / \gamma_x^s) = 8.77$  which

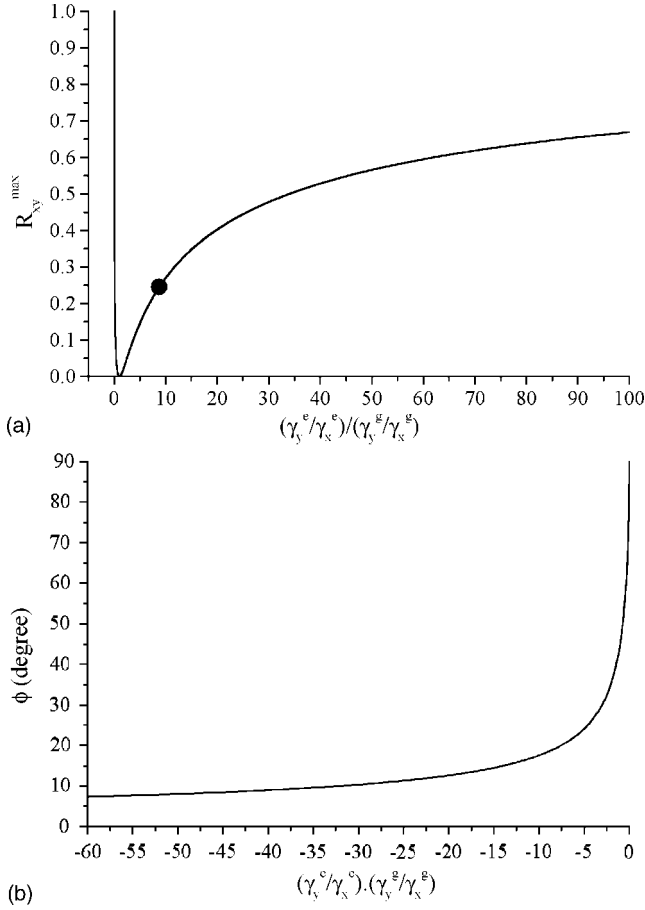


FIG. 8. (a) Maximum transition strength ratio  $R_{xy}^{\max}$  in the  $x$ - $y$  plane as a function of  $(\gamma_y^e/\gamma_x^e)/(\gamma_y^g/\gamma_x^g)$  when  $[(\gamma_y^e/\gamma_x^e)(\gamma_y^g/\gamma_x^g)]$  is positive. The black circle corresponds to the case of Tm:YAG. (b) Angle  $\phi$  of the external magnetic field ( $\theta=90^\circ$ ) as a function of  $(\gamma_y^e/\gamma_x^e)(\gamma_y^g/\gamma_x^g)$  giving a transition strength ratio  $R_{xy}=1$  when  $[(\gamma_y^e/\gamma_x^e)(\gamma_y^g/\gamma_x^g)]$  is negative.

gives  $R_{xy}^{\max}=0.24$  for a  $\mathbf{B}_0$  orientation of  $\theta=90^\circ$  and  $\phi=5.7^\circ$ . These results are exactly the ones we have obtained from the complete crystal-field Hamiltonian approach.

When  $(\gamma_y^e/\gamma_x^e)(\gamma_y^g/\gamma_x^g)$  is negative, we can always find a  $\mathbf{B}_0$  orientation which fulfills the  $((\gamma_y^e/\gamma_x^e)(\gamma_y^g/\gamma_x^g))(B_0^y/B_0^x)^2=-1$  condition. The angle  $\phi$  which gives  $R_{xy}=1$  is

$$\phi = \arctan \frac{1}{\sqrt{-\frac{\gamma_y^e \gamma_y^g}{\gamma_x^e \gamma_x^g}}}. \quad (33)$$

$\phi$  is plotted in Fig. 8(b) as a function of  $(\gamma_y^e/\gamma_x^e)(\gamma_y^g/\gamma_x^g)$ . For large values of  $(\gamma_y^e/\gamma_x^e)(\gamma_y^g/\gamma_x^g)$ , small angles of  $\phi$  give  $R_{xy}=1$ . For small values of  $(\gamma_y^e/\gamma_x^e)(\gamma_y^g/\gamma_x^g)$ , large values of  $\phi$  are needed.

To conclude, the spin-Hamiltonian approach allows us to explain the results of the complete calculation performed in Sec. II. Moreover it allows us to find a condition to obtain an ideal three-level  $\Lambda$  system with  $\text{Tm}^{3+}$  ions for hosts in which the  $\text{Tm}^{3+}$  ions are characterized by a negative  $(\gamma_y^e/\gamma_x^e)(\gamma_y^g/\gamma_x^g)$  ratio.

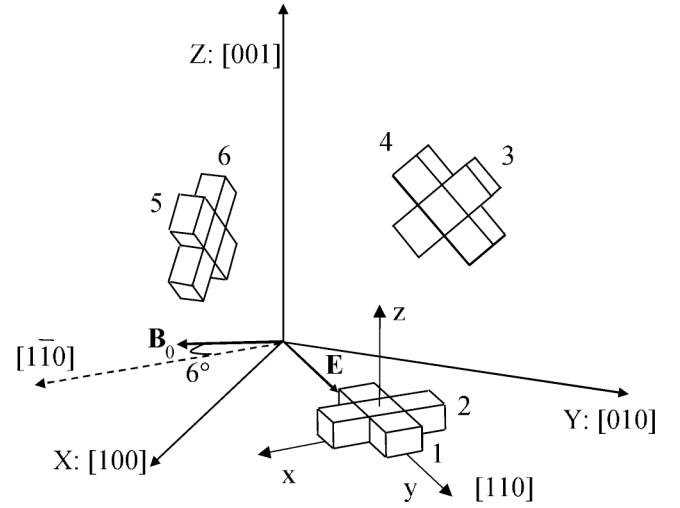


FIG. 9. Arrangement of the six orientationally nonequivalent sites with respect to the crystallographic axes, from Ref. 38. The magnetic field  $\mathbf{B}_0$  lies in the horizontal plane, at  $6^\circ$  from direction  $[1\bar{1}0]$ , in order to optimize the transition strength ratio  $R$  in site 1. The light field  $\mathbf{E}$  is aligned along site 1 transition dipole moment, which maximizes interaction with ions in this site.

#### IV. EXPERIMENTAL PROTOCOL

In this section we describe an experimental protocol that makes a crystal similar to the atomic samples used in previous quantum information investigations, with the additional benefits of absence of motion and long coherence time. This will complete our demonstration that such experiments are feasible in thulium doped YAG.

We have to prepare the crystal in such a way that absorption at a given frequency be ascribed to a single class of ions, exhibiting the same three-level  $\Lambda$  system, with the same level spacing and the same transition strength on each one of the two lines. Initially various classes of ions are absorbing at a given frequency. This results from the frequency shift caused by the crystalline field and from the existence of non-equivalent sites.

There are six types of dodecahedral sites in YAG, each having the same crystallographic symmetry when referred to the  $(x, y, z)$  local axes, which are, however, orientationally nonequivalent sites. Their relative orientation with respect to the  $(X, Y, Z)$  crystallographic axes is illustrated in Fig. 9, following Ref. 38. We take the notation of Ref. 38 to number the different sites: sites 1 and 2 are in the  $X$ - $Y$  crystallographic plane, sites 3 and 4 are in the  $Y$ - $Z$  plane, and sites 5 and 6 are in the  $X$ - $Z$  plane. When an external magnetic field is applied, the six sites generally become nonequivalent, which means they are characterized by different hyperfine splittings and different values of the transition strength ratio  $R$ . We can take advantage of the different splitting values to select ions in a specific site, with optimized transition strength ratio.

From the previous local orientation of  $\mathbf{B}_0$  ( $\theta=90^\circ$  and  $\phi=6^\circ$ ) which gives the best  $\Lambda$  system for Tm:YAG, we obtain the corresponding orientation  $(\theta_{XYZ}, \phi_{XYZ})$  in the crystallographic axes for the six sites:

TABLE III. Hyperfine splitting, transition strength ratio, and angle between the two effective magnetic fields for the six magnetically inequivalent sites of  $\text{Tm}^{3+}$  in YAG for an orientation of the applied magnetic field of  $\theta_{XYZ}=90^\circ$  and  $\phi_{XYZ}=-51^\circ$  in the crystallographic axes.

Site	Splitting (MHz)		$R$	$\alpha^{eff}$ (deg)
	${}^3H_6(0)$	${}^3H_4(0)$		
1	60.7	22.3	0.24	52.2
2	536.8	71.5	$1.10^{-4}$	1.5
3	301.6	41.4	0.02	14.9
4	301.6	41.4	0.02	14.9
5	244.9	33.7	0.02	15.5
6	244.9	33.7	0.02	15.5

- $n^\circ 1: \theta_{XYZ}=90^\circ, \phi_{XYZ}=-39^\circ$  or  $-51^\circ,$
- $n^\circ 2: \theta_{XYZ}=90^\circ, \phi_{XYZ}=+39^\circ$  or  $+51^\circ,$
- $n^\circ 3: \theta_{XYZ}=39^\circ$  or  $51^\circ, \phi_{XYZ}=-90^\circ,$
- $n^\circ 4: \theta_{XYZ}=39^\circ$  or  $51^\circ, \phi_{XYZ}=+90^\circ,$
- $n^\circ 5: \theta_{XYZ}=-39^\circ$  or  $-51^\circ, \phi_{XYZ}=0^\circ,$
- $n^\circ 6: \theta_{XYZ}=+39^\circ$  or  $+51^\circ, \phi_{XYZ}=0^\circ.$

Let us assume we optimize  $R$  in site 1. This corresponds to the orientation:  $\theta_{XYZ}=90^\circ$  and  $\phi_{XYZ}=39^\circ$  or  $51^\circ$  with respect to the crystallographic axes. To maximize the incident light interaction with site 1, we align the electromagnetic field polarization along the site transition dipole moment that is directed along  $\theta_{XYZ}=90^\circ$  and  $\phi_{XYZ}=45^\circ$ . The field propagates along the  $[1\bar{1}0]$  direction. The field arrangement is summarized in Fig. 9. The different hyperfine splittings,  $\alpha^{eff}$ , and  $R=\tan^2(\alpha^{eff}/2)$  values are summarized in Table III for this specific magnetic-field orientation. Hyperfine splitting in site 1 appears to be much smaller than in the other sites, while the transition ratio is much larger in site 1. The dipole moment of the  $|1\rangle \rightarrow |3\rangle$  transition can be written as  $\mu \cos(\alpha^{eff}/2)$  where  $\mu$  is the electric transition dipole moment. In sites 2–6, this quantity is close to  $\mu$  and equals  $0.90\mu$  in site 1. The site 2 dipole moment is cross-polarized with the incident light and does not interact with it.

Let us define  $\nu_0$  as the mean  ${}^3H_6(0) \rightarrow {}^3H_4(0)$  transition frequency and let  $\Delta_i^{(g)}$  and  $\Delta_i^{(e)}$ , respectively, represent the hyperfine splitting of the ground and excited electronic states in site  $i$ . Because of site degeneracy,  $\Delta_3^{(e,g)}=\Delta_4^{(e,g)}$  and  $\Delta_5^{(e,g)}=\Delta_6^{(e,g)}$ . An incident light beam at frequency  $\nu_L$  is resonant with the various  $\nu_0$  classes that satisfy one of the conditions:

$$\nu_0 = \nu_L \pm \frac{1}{2}\Delta_i^{(g)} \pm \frac{1}{2}\Delta_i^{(e)} \quad (34)$$

as illustrated in Fig. 10. Given the partial site degeneracy, 12 different values of  $\nu_0$  satisfy this resonance condition.

Ion selection procedures were used successfully in the past.<sup>14,16,39</sup> We propose to follow similar lines of operation to select a single group of ions. One first bleaches the sample at frequency  $\nu_L$ , the ground-state sublevel being emptied by

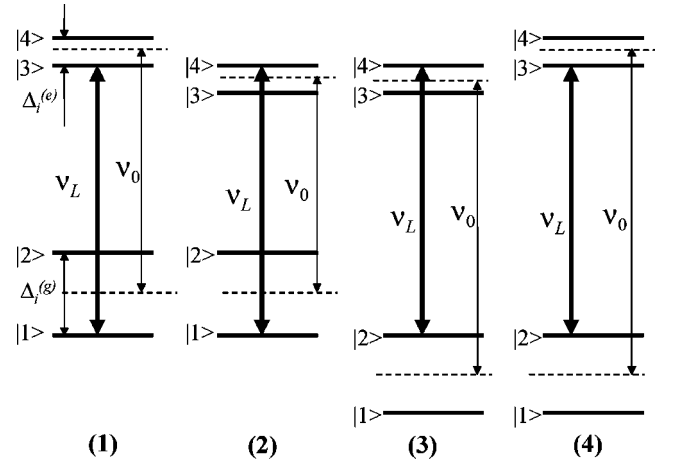


FIG. 10. Energy-level schemes of ions that resonantly interact with the incident light field at frequency  $\nu_L$ . In each site, four different groups of ions, with four different values of the mean transition frequency  $\nu_0$ , are simultaneously excited by the light field. The represented schemes correspond to site  $i$ , as indicated by the sublevel splitting label. Similar schemes can be drawn for each one of the six sites. Given the partial site degeneracy and the absence of excitation in site 2, there is a total of 12 different schemes to be considered. In each set the schemes are labeled from  $k=1$  to 4. Strongest coupling at  $\nu_L$  occurs in schemes 1 and 3. In schemes 2 and 4, coupling is stronger at  $\nu_L - \Delta_i^{(g)}$  and  $\nu_L + \Delta_i^{(e)}$ , respectively.

optical pumping to the other sublevel. The stepwise pumping process proceeds through excitation to the upper state of the optical transition, followed by nonradiative decay to the long lifetime  ${}^3F_4$  state and ultimate decay to ground state after 10 ms storage in  ${}^3F_4$ . The procedure works because the ground-state hyperfine structure population lifetime can reach several minutes in  $\text{Tm}^{3+}:\text{YAG}$  under moderate magnetic field, as demonstrated in Ref. 22. After this bleaching step, ions initially resonant at  $\nu_L$  are now resonant at the six different frequencies  $\nu_L \pm \Delta_i^{(g)}$ . Then one proceeds with distillation by bleaching the sample at frequency  $\nu_L - \Delta_1^{(g)}$ . The excited ions are optically pumped to the other sublevel where they are resonant at frequency  $\nu_L - \Delta_1^{(g)} \pm \Delta_i^{(g)}$ . Therefore this step returns site 1 ions, and only these, to frequency  $\nu_L$ . At this step the situation is the following: the frequency slot at  $\nu_L - \Delta_1^{(g)}$  is empty and the slot at  $\nu_L$  is only occupied by site 1 ions. The three-level systems will be controlled at frequencies  $\nu_L - \Delta_1^{(g)}$  and  $\nu_L$ . It should be stressed that, by selecting  $\nu_L - \Delta_1^{(g)}$  as the control frequency, one disregarded the site 1 ions that were pumped to frequency  $\nu_L + \Delta_1^{(g)}$  in the first bleaching step. Half of the initial site 1 population at  $\nu_L$  is lost. The distillation is not yet complete as illustrated in Fig. 11. Half of the selected ions are also resonant at  $\nu_L + \Delta_1^{(e)}$  and  $\nu_L - \Delta_1^{(g)} + \Delta_1^{(e)}$ , and the other half at  $\nu_L - \Delta_1^{(g)}$  and  $\nu_L - \Delta_1^{(g)} - \Delta_1^{(e)}$ . These two ion groups interact differently with the incident light. In the former set the Rabi frequency is larger at  $\nu_L$  than at  $\nu_L - \Delta_1^{(g)}$ . The opposite situation prevails in the latter set. In order to keep ions with the same well-defined Rabi frequencies, one can pump the other ones to the shelving state  ${}^3F_4$ . This can be accomplished by excitation at  $\nu_L - \Delta_1^{(e)}$ . The selection is time-limited to the 10 ms lifetime of  ${}^3F_4$ .

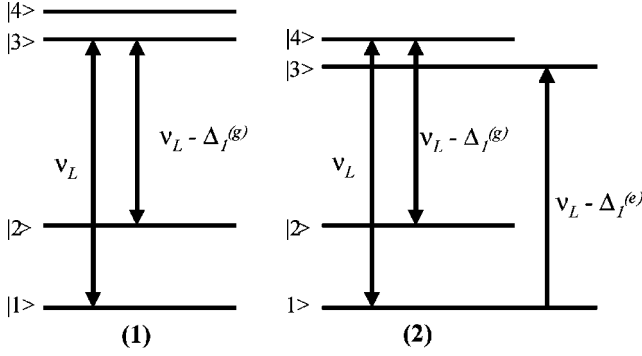


FIG. 11. Energy level schemes of the two ion sets selected by successive optical pumping at  $\nu_L$  and  $\nu_L - \Delta_I^{(g)}$ . To keep a single set, one temporarily stores the other one on the shelving state  ${}^3F_4$ . In the picture, one only keeps the set (1) and one pumps the other one to  ${}^3F_4$  by optical excitation at  $\nu_L - \Delta_I^{(e)}$ .

In order to keep all the selected ions, one must bleach the sample over a spectral interval larger than the inhomogeneous width of the Zeeman transition. This broadening is expected not to exceed a few tens of kilohertz.

Optical density often appears to be a key parameter in quantum information storage experiments. To evaluate this quantity we assume that the magnetic field does not affect the electric dipole line strength  $X$ . Then the optical density can be expressed as:

$$D \propto \sum_{i \in 1}^6 \sum_{k=1}^4 X_i^{(k)}, \quad (35)$$

where the sums run over the six sites and the four diagrams of Fig. 10, and  $X_i^{(k)}$  is defined as

$$X_i^{(k)} = \begin{cases} X[\cos \theta_i \cos(\alpha_i^{eff}/2)]^2, & k = 1, 3 \\ X[\cos \theta_i \sin(\alpha_i^{eff}/2)]^2, & k = 2, 4, \end{cases} \quad (36)$$

where  $\theta_i$  stands for the angle between the excitation field and the transition dipole moment in site  $i$ . This angle takes on the following values:  $\theta_1=0^\circ$ ,  $\theta_2=90^\circ$ ,  $\theta_{3..6}=60^\circ$  and  $\alpha_i^{eff}$  values are summarized in Table III. Finally, the relative optical density of the selected ion group amounts to

$$\frac{D_1^{(1)}}{D} = \frac{X_1^{(1)}}{\sum_{i=1}^6 \sum_{k=1}^4 X_i^{(k)}} = 0.20. \quad (37)$$

Selection of a single class of ions reduces the optical density to 0.20 times its initial value. In the concentration conditions of Ref. 22 (0.5 at. %  $\text{Tm}^{3+}$ :YAG), the linear absorption coefficient is  $\sim 10 \text{ cm}^{-1}$ , which leads to a single-site contribution of  $\sim 2.5 \text{ cm}^{-1}$ . In the quantum storage experiment presented in Ref. 5, performed in a caesium atom magneto-optic trap, the absorption is  $\sim 4\text{--}5 \text{ cm}^{-1}$ , which could be obtained with a 2 cm thick sample of  $\text{Tm}^{3+}$ :YAG.

## V. CONCLUSION

The magnetic interactions in rare-earth-doped crystals have been studied under an external magnetic field in order

to obtain an efficient three-level  $\Lambda$  system.  $\text{Tm}^{3+}$  ions appear to be a good candidate for such purpose. The particular case of  $\text{Tm}$ :YAG has been discussed. A complete crystal-field calculation has been performed as well as an analytical analysis of the results based on a spin-Hamiltonian approach. For time inversion symmetry reason, the  $\text{Tm}$ :YAG energy levels do not exhibit hyperfine splitting under hyperfine interaction alone. Nuclear Zeeman effect under the action of an external magnetic field removes the nuclear degeneracy. This still does not provide us with a  $\Lambda$ -type three-level system because nuclear-spin flipping such as  $M_I({}^3H_6) = \pm \frac{1}{2} \rightarrow M_I({}^3H_4) = \mp \frac{1}{2}$  cannot be induced by an optical transition. However, this selection rule only applies to pure nuclear Zeeman effect. The dominant effect for the splitting of the hyperfine levels comes from the coupling of the electronic Zeeman and hyperfine interactions. This can be described in terms of a pseudonuclear Zeeman interaction induced by an effective magnetic field. Optical transition with nuclear-spin flipping can take place as soon as the effective magnetic-field orientation is different in the ground and excited states. The relative orientation of the effective fields depends on the applied field orientation. We have found that for  $\text{Tm}^{3+}$  ions which have a nuclear spin of  $1/2$ , a transition strength ratio  $R=1$  can be obtained in the  $x$ - $y$  plane when the spin-Hamiltonian parameters give a negative  $(\gamma_y^e/\gamma_x^e)(\gamma_y^g/\gamma_x^g)$  ratio.

In the case of  $\text{Tm}$ :YAG, the best three-level  $\Lambda$  system is obtained with an applied magnetic-field orientation of  $\theta = 90^\circ$  and  $\phi = 6^\circ$  in the local crystal-field axes which gives  $52^\circ$  of relative orientation between the effective fields associated to the ground and excited states and a transition strength ratio  $R=0.24$ . These results have been understood in the spin-Hamiltonian formalism.

Finally, we describe an experimental protocol which allows us to prepare the crystal in such a way that absorption at a given frequency be ascribed to a single class of ions, exhibiting the same three-level  $\Lambda$  system, with the same level spacing and the same transition strength on each one of the two lines. The relative optical density of the selected ion group amounts to 0.20 times its initial value, and an absorption of  $4\text{--}5 \text{ cm}^{-1}$  could be obtained with a 2 cm thick sample of 0.5 at. %  $\text{Tm}^{3+}$ :YAG.

## ACKNOWLEDGMENT

This work was carried out under the ESQUIRE project supported by the IST-FET program of the EC.

## APPENDIX: MATRIX ELEMENTS OF MAGNETIC INTERACTIONS

### 1. Electronic Zeeman interaction

The electronic Zeeman interaction in tensorial notation reads

$$\begin{aligned} H_{EZ} &= \beta[B_{0x}(\mathbf{L} + g_s\mathbf{S})_x + B_{0y}(\mathbf{L} + g_s\mathbf{S})_y + B_{0z}(\mathbf{L} + g_s\mathbf{S})_z] \\ &= \beta \left[ (\mathbf{L} + g_s\mathbf{S})_{-1}^{(1)} \left( \frac{B_{0x} + iB_{0y}}{\sqrt{2}} \right) + (\mathbf{L} + g_s\mathbf{S})_1^{(1)} \right. \\ &\quad \left. \times \left( \frac{-B_{0x} + iB_{0y}}{\sqrt{2}} \right) + (\mathbf{L} + g_s\mathbf{S})_0^{(1)} B_{0z} \right], \end{aligned} \quad (A1)$$

where  $(\mathbf{L} + g_s \mathbf{S})_{-1,0,1}^{(1)}$  are the different components of the tensor operator  $(\mathbf{L} + g_s \mathbf{S})^{(1)}$  of rank 1. The applied magnetic field is given in the local crystal-field axis set  $(x, y, z)$ . The matrix elements of the electronic Zeeman interaction in the  $LS$  coupling may be obtained by using the Wigner-Eckart theorem to yield

$$\langle \gamma SLJM_J IM_I | H_{EZ} | \gamma' S' L' J' M'_J IM'_I \rangle = \beta \left[ \begin{aligned} & (-1)^{J-M_J} \begin{pmatrix} J & 1 & J' \\ -M_J & -1 & M'_J \end{pmatrix} \left( \frac{B_{0x} + iB_{0y}}{\sqrt{2}} \right) \\ & + (-1)^{J-M_J} \begin{pmatrix} J & 1 & J' \\ -M_J & 1 & M'_J \end{pmatrix} \left( \frac{-B_{0x} + iB_{0y}}{\sqrt{2}} \right) \\ & + (-1)^{J-M_J} \begin{pmatrix} J & 1 & J' \\ -M_J & -1 & M'_J \end{pmatrix} B_{0z} \end{aligned} \right] \\ \times \delta(M_I, M'_I) \langle \gamma SLJ || (\mathbf{L} + g_s \mathbf{S})^{(1)} || \gamma' S' L' J' \rangle,$$

where

$$\begin{pmatrix} J & 1 & J' \\ -M_J & q & M'_J \end{pmatrix}$$

is a 3- $j$  symbol and  $\langle \gamma SLJ || (\mathbf{L} + g_s \mathbf{S})^{(1)} || \gamma' S' L' J' \rangle$  is the reduced matrix element of the  $(\mathbf{L} + g_s \mathbf{S})^{(1)}$  operator. This reduced matrix element is

$$\langle \gamma SLJ || (\mathbf{L} + g_s \mathbf{S})^{(1)} || \gamma' S' L' J' \rangle = \delta(J, J') \delta(L, L') \delta(S, S') \delta(\gamma, \gamma') \sqrt{J(J+1)[J]} + (-1)^{S+L+J'+1} \delta(L, L') \delta(S, S') \delta(\gamma, \gamma') \sqrt{[J][J']} \\ \times \left\{ \begin{matrix} J & 1 & J' \\ S & L & S \end{matrix} \right\} (g_s - 1) \sqrt{S(S+1)[S]},$$

where

$$\left\{ \begin{matrix} J & 1 & J' \\ S & L & S \end{matrix} \right\}$$

is a 6- $j$  symbol. The expression in square brackets  $[J]$  means  $2J+1$ .

## 2. Hyperfine interaction

In tensorial notation, the hyperfine interaction is written as

$$H_{HF} = a_I \sum_{i=1}^N [\mathbf{I}_i^{(1)} - \sqrt{10} (\mathbf{sC}^{(2)})_i^{(1)}] \cdot \mathbf{I}^{(1)} = a_I \sum_{i=1}^N \mathbf{N}_i^{(1)} \cdot \mathbf{I}^{(1)} \quad (\text{A2})$$

with  $a_I = g_s \beta \beta_n g_I \langle r_e^{-3} \rangle$ ,  $\langle r_e^{-3} \rangle$  is the inverse-cube radius of the electron orbital. The matrix elements of the hyperfine interaction are

$$\langle \gamma LSJM_J IM_I | H_{HF} | \gamma' L' S' J' M'_J IM'_I \rangle = a_I \left[ \begin{aligned} & (-1)^{J-M_J} \begin{pmatrix} J & 1 & J' \\ -M_J & 0 & M'_J \end{pmatrix} (-1)^{I-M_I} \begin{pmatrix} I & 1 & I \\ -M_I & 0 & M'_I \end{pmatrix} \\ & - (-1)^{J-M_J} \begin{pmatrix} J & 1 & J' \\ -M_J & 1 & M'_J \end{pmatrix} (-1)^{I-M_I} \begin{pmatrix} I & 1 & I \\ -M_I & -1 & M'_I \end{pmatrix} \\ & - (-1)^{J-M_J} \begin{pmatrix} J & 1 & J' \\ -M_J & -1 & M'_J \end{pmatrix} (-1)^{I-M_I} \begin{pmatrix} I & 1 & I \\ -M_I & 1 & M'_I \end{pmatrix} \end{aligned} \right] \\ \times \langle \gamma LSJ || \sum_{i=1}^N \mathbf{N}_i^{(1)} || \gamma' L' S' J' \rangle \langle I || I^{(1)} || I \rangle$$

with

$$\langle I || I^{(1)} || I \rangle = \sqrt{I(I+1)[I]}$$

and

$$\langle \gamma LSJ \| \left( \sum_{i=1}^N \mathbf{N}_i \right)^{(1)} \| \gamma' L' S' J' \rangle = (-1)^{L+S+J'+1} \delta(S, S') \delta(L, L') \delta(\gamma, \gamma') \sqrt{L(L+1)[L]} \sqrt{[J][J']} \begin{Bmatrix} J & 1 & J' \\ L & S & L \end{Bmatrix} \\ - \sqrt{3} \langle f | C^{(2)} | f \rangle \sqrt{[J][J']} \begin{Bmatrix} S & S' & 1 \\ L & L' & 2 \\ J & J' & 1 \end{Bmatrix} \langle \gamma SL \| W^{(12)} \| \gamma' S' L' \rangle,$$

where

$$\begin{Bmatrix} J & 1 & J' \\ L & S & L \end{Bmatrix}$$

and

$$\begin{Bmatrix} S & S' & 1 \\ L & L' & 2 \\ J & J' & 1 \end{Bmatrix}$$

are a 6- $j$  and 9- $j$  symbols and

$$\langle f | C^{(2)} | f \rangle = (-1)^3 [3] \begin{pmatrix} 3 & 2 & 3 \\ 0 & 0 & 0 \end{pmatrix}.$$

The  $\langle \gamma SL \| W^{(12)} \| \gamma' S' L' \rangle$  matrix elements are given in the Nielson and Koster table.<sup>40</sup>

### 3. Nuclear Zeeman interaction

The nuclear Zeeman interaction in tensorial notation is

$$H_{NZ} = -g_n \beta_n [B_{0x} \mathbf{I}_x + B_{0y} \mathbf{I}_y + B_{0z} \mathbf{I}_z] \\ = -g_n \beta_n \begin{bmatrix} \mathbf{I}_{-1}^{(1)} \left( \frac{B_{0x} + iB_{0y}}{\sqrt{2}} \right) \\ + \mathbf{I}_1^{(1)} \left( \frac{-B_{0x} + iB_{0y}}{\sqrt{2}} \right) \\ + \mathbf{I}_0^{(1)} B_{0z} \end{bmatrix},$$

which gives the following matrix elements in the  $|\gamma LSJM_J IM_I\rangle$  basis set:

$$\langle \gamma SLJM_J IM_I | H_{NZ} | \gamma' S' L' J' M'_J IM'_I \rangle$$

$$= -g_n \beta_n \begin{bmatrix} (-1)^{I-M_I} \begin{pmatrix} I & 1 & I \\ -M_I & -1 & M'_I \end{pmatrix} \left( \frac{B_{0x} + iB_{0y}}{\sqrt{2}} \right) \\ + (-1)^{I-M_I} \begin{pmatrix} I & 1 & I \\ -M_I & 1 & M'_I \end{pmatrix} \left( \frac{-B_{0x} + iB_{0y}}{\sqrt{2}} \right) \\ + (-1)^{I-M_I} \begin{pmatrix} I & 1 & I \\ -M_I & 0 & M'_I \end{pmatrix} B_{0z} \end{bmatrix} \\ \times \langle \gamma SLJM_J I | \mathbf{I}^{(1)} | \gamma' S' L' J' M'_J I \rangle$$

with

$$\langle \gamma SLJM_J I | \mathbf{I}^{(1)} | \gamma' S' L' J' M'_J I \rangle \\ = \delta(\gamma, \gamma') \delta(S, S') \delta(L, L') \delta(J, J') \delta(M_J, M'_J) \sqrt{I(I+1)[I]}.$$

### 4. Electric quadrupole interaction

In the case of  $\text{Tm}^{3+}$  ions, this interaction does not exist but as we want to apply this work to all the possible non-Kramers ions, we also give the matrix elements of this interaction in the  $|\gamma LSJM_J IM_I\rangle$  basis set. To express the electric quadrupole interaction in the tensorial notation, we have first to expand the  $1/|r_e - r_n|$  denominator in terms of spherical harmonics  $Y_{kq}$  by

$$\frac{1}{|r_e - r_n|} = \sum_k r_n^k \left[ \sum_i \left( \frac{1}{r_{ei}^{k+1}} C_{ei}^{(k)} \right) C_n^{(k)} \right]$$

with

$$C_q^{(k)} = \sqrt{\frac{4\pi}{2k+1}} Y_{kq}.$$

By symmetry considerations, the terms corresponding to odd values of  $k$  are zero, the terms with  $k=2$  correspond to the electric quadrupole interaction.<sup>30</sup> If we neglect the terms with  $k>2$ ,  $H_Q$  can then be written as

$$H_Q = -e^2 \int \int \rho_e(r_e) \rho_n(r_n) \sum_i (r_{ei}^{-3} C_{ei}^{(2)}) (r_n^2 C_n^{(2)}) d\tau_e d\tau_n, \quad (\text{A3})$$

which gives the following matrix elements:

$$\langle \gamma L S J M_J M_I | H_Q | \gamma' L' S' J' M'_J M'_I \rangle = (-e^2) \left[ \begin{array}{l} (-1)^{J-M_J} \begin{pmatrix} J & 2 & J' \\ -M_J & 0 & M'_J \end{pmatrix} (-1)^{I-M_I} \begin{pmatrix} I & 2 & I \\ -M_I & 0 & M'_I \end{pmatrix} \\ - (-1)^{J-M_J} \begin{pmatrix} J & 2 & J' \\ -M_J & 1 & M'_J \end{pmatrix} (-1)^{I-M_I} \begin{pmatrix} I & 2 & I \\ -M_I & -1 & M'_I \end{pmatrix} \\ - (-1)^{J-M_J} \begin{pmatrix} J & 2 & J' \\ -M_J & -1 & M'_J \end{pmatrix} (-1)^{I-M_I} \begin{pmatrix} I & 2 & I \\ -M_I & 1 & M'_I \end{pmatrix} \\ + (-1)^{J-M_J} \begin{pmatrix} J & 2 & J' \\ -M_J & -2 & M'_J \end{pmatrix} (-1)^{I-M_I} \begin{pmatrix} I & 2 & I \\ -M_I & 2 & M'_I \end{pmatrix} \\ + (-1)^{J-M_J} \begin{pmatrix} J & 2 & J' \\ -M_J & 2 & M'_J \end{pmatrix} (-1)^{I-M_I} \begin{pmatrix} I & 2 & I \\ -M_I & -2 & M'_I \end{pmatrix} \end{array} \right] \\ \times \langle \gamma L S J | \sum_i (r_{ei}^{-3} C_{ei}^{(2)}) | \gamma' L' S' J' \rangle \langle I | r_n^2 C_n^{(2)} | I \rangle$$

with

$$\langle I | r_n^2 C_n^{(2)} | I \rangle = Q \left( \frac{I(2I-1)}{(I+1)(2I+1)(2I+3)} \right)^{-1/2}$$

and

$$\langle \gamma L S J | \sum_i (r_{ei}^{-3} C_{ei}^{(2)}) | \gamma' L' S' J' \rangle = \langle r_e^{-3} \rangle (-1)^{L+S+J'+2} \delta(S, S') \sqrt{[J][J']} \begin{Bmatrix} J & 2 & J' \\ L' & S & L \end{Bmatrix} (-1)^3 [3] \begin{pmatrix} 3 & 2 & 3 \\ 0 & 0 & 0 \end{pmatrix} \langle \gamma L | U^{(2)} | \gamma' L' \rangle.$$

$Q$  is the nuclear quadrupole moment. The reduced  $\langle \gamma L | U^{(2)} | \gamma' L' \rangle$  matrix elements are given in the Nielson and Koster table.<sup>40</sup>

\*Author to whom correspondence should be addressed. Electronic address: guillotn@ext.jussieu.fr

<sup>1</sup>J. Hald, J. L. Sørensen, C. Schori, and E. S. Polzik, Phys. Rev. Lett. **83**, 1319 (1999).

<sup>2</sup>A. Kuzmich, L. Mandel, and N. P. Bigelow, Phys. Rev. Lett. **85**, 1594 (2000).

<sup>3</sup>B. Julsgaard, A. Kozhekin, and E. S. Polzik, Nature (London) **413**, 400 (2001).

<sup>4</sup>C. H. van der Wal, M. D. Eisaman, A. André, R. L. Walsworth, D. F. Phillips, A. S. Zibrov, and M. D. Lukin, Science **301**, 196 (2003).

<sup>5</sup>A. Kuzmich, W. P. Bowen, A. D. Boozer, A. Boca, C. W. Chou, L.-M. Duan, and H. J. Kimble, Nature (London) **423**, 731 (2003).

<sup>6</sup>M. Fleischhauer and M. D. Lukin, Phys. Rev. Lett. **84**, 5094 (2000).

<sup>7</sup>G. Alzetta, A. Gozzini, L. Moi, and G. Orriols, Nuovo Cimento B **36**, 5 (1976).

<sup>8</sup>S. E. Harris, Phys. Today **50**(7), 36 (1997).

<sup>9</sup>D. F. Phillips, A. Fleischhauer, A. Mair, R. L. Walsworth, and M. D. Lukin, Phys. Rev. Lett. **86**, 783 (2001).

<sup>10</sup>N. V. Vitanov, M. Fleischhauer, B. W. Shore, and K. Bergmann, Adv. At., Mol., Opt. Phys. **46**, 55 (2001).

<sup>11</sup>R. M. Macfarlane and R. M. Shelby, *Spectroscopy of Solids Containing Rare Earth Ions*, edited by A. A. Kaplyanski and R. M. Macfarlane (North Holland, Amsterdam, 1987), p. 51.

<sup>12</sup>E. Fraval, M. J. Sellars, and J. J. Longdell, Phys. Rev. Lett. **92**, 077601 (2004).

<sup>13</sup>B. S. Ham, P. R. Hemmer, and M. S. Shahriar, Opt. Commun. **144**, 227 (1997).

<sup>14</sup>B. S. Ham, P. R. Hemmer, and M. S. Shahriar, Phys. Rev. A **59**, R2583 (1999).

<sup>15</sup>A. V. Turukhin, V. S. Sudarshanam, M. S. Shariar, J. A. Musser, B. S. Ham, and P. R. Hemmer, Phys. Rev. Lett. **88**, 023602 (2002).

<sup>16</sup>R. M. Macfarlane, J. Lumin. **100**, 1 (2002).

<sup>17</sup>Ph. Goldner and O. Guillot-Noël, Mol. Phys. **102**, 1185 (2004).

<sup>18</sup>M. Mitsunaga, N. Uesugi, and K. Sugiyama, Opt. Lett. **18**, 1256 (1993).

<sup>19</sup>M. J. Sellars, R. S. Meltzer, P. T. H. Fisk, and N. B. Manson, J. Opt. Soc. Am. B **11**, 1468 (1994).

<sup>20</sup>R. Klieber, A. Michalowski, R. Neuhaus, and D. Suter, Phys. Rev. B **67**, 184103 (2003).

<sup>21</sup>N. Ohlsson, M. Nilsson, S. Kröll, and R. Krishna Mohan, Opt. Lett. **28**, 450 (2003).

<sup>22</sup>Z. Cole, T. Böttger, R. Krishna Mohan, R. Reibel, W. R. Babbitt, R. L. Cone, and K. D. Merkel, Appl. Phys. Lett. **81**, 3525 (2002).

<sup>23</sup>V. Lavielle, I. Lorgeré, J.-L. Le Gouët, S. Tonda, and D. Dolfi, Opt. Lett. **28**, 384 (2003).

<sup>24</sup>R. M. Macfarlane, Opt. Lett. **18**, 1958 (1993).

<sup>25</sup>A. Schoof, J. Grünert, S. Ritter, and A. Hemmerich, Opt. Lett. **26**, 1562 (2001), and references therein.

<sup>26</sup>D. P. McLeod and M. F. Reid, J. Alloys Compd. **250**, 302 (1997).

<sup>27</sup>G. D. Jones and N. M. Strickland, J. Lumin. **102–103**, 166 (2003).

- <sup>28</sup>F. Ramaz, R. M. Macfarlane, J. C. Vial, J. P. Chaminade, and F. Madéore, *J. Lumin.* **55**, 173 (1993).
- <sup>29</sup>W. T. Carnall, G. L. Goodman, K. Rajnak, and R. S. Rana, *J. Chem. Phys.* **90**, 3443 (1989).
- <sup>30</sup>B. G. Wybourne, *Spectroscopic Properties of Rare Earths* (Interscience, New York, 1965).
- <sup>31</sup>B. R. Judd, *Operator Techniques in Atomic Spectroscopy* (McGraw-Hill, New York, 1963), p. 85.
- <sup>32</sup>C. Tiseanu, A. Lupei, and V. Lupei, *J. Phys.: Condens. Matter* **7**, 8477 (1995).
- <sup>33</sup>J. B. Gruber, M. E. Hills, R. M. Macfarlane, C. A. Morrison, G. A. Turner, G. J. Quarles, G. J. Klintz, and L. Esterowitz, *Phys. Rev. B* **40**, 9464 (1989).
- <sup>34</sup>A. Abragam and B. Bleaney, *Electron Paramagnetic Resonance of Transition Ions* (Dover, New York, 1986).
- <sup>35</sup>M. A. Teplov, *Zh. Eksp. Teor. Fiz.* **53**, 1510 (1967); [*Sov. Phys. JETP* **26**, 872 (1968)].
- <sup>36</sup>K. K. Sharma and L. E. Erickson, *Phys. Rev. Lett.* **45**, 294 (1980).
- <sup>37</sup>L. E. Erickson, *Phys. Rev. B* **32**, 1 (1985).
- <sup>38</sup>L. F. Johnson, J. F. Dillon, and J. P. Remeika, *Phys. Rev. B* **1**, 1935 (1970).
- <sup>39</sup>M. Nilsson, L. Rippe, S. Kröll, R. Klieber, and D. Suter, ArXiv cond-mat/0408515 (unpublished).
- <sup>40</sup>C. W. Nielson and G. F. Koster, *Spectroscopic Coefficients for the  $p^n$ ,  $d^n$  and  $f^n$  Configurations* (MIT, Cambridge, 1963).